

Chemically Anomalous, Preaccretionally Irradiated Grains in Interplanetary Dust from Comets

John P. Bradley

Nonstoichiometric grains with depletions of magnesium and silicon (relative to oxygen) and inclusions of iron-nickel metal and iron-rich sulfides have been identified in interplanetary dust particles from comets. These chemical anomalies accumulate in grains exposed to ionizing radiation. The grains, known as GEMS (glass with embedded metal and sulfides), were irradiated before the accretion of comets, and their inferred exposure ages, submicrometer sizes, and "amorphous" silicate structures are consistent with those of interstellar silicate grains. The measured compositional trends suggest that chemical (as well as isotopic) anomalies can be used to identify presolar interstellar components in primitive meteoritic materials.

Although dust constitutes <1% of the mass of the interstellar medium (H and He provide most of the mass), it plays a fundamental role in physical and chemical processes occurring throughout the galaxy (1). Dust grains are produced mainly by condensation in the expanding atmospheres of cool giant stars and are observed in planetary nebulas, novae, protostellar nebulas, and the ejecta of supernovas (2). The properties of interstellar dust are variable, depending on local environments within the interstellar medium, but C-rich grains and "amorphous" silicates, with diameters between 0.1 and 1 μm , are major constituents (1-4). Interstellar grains of C (graphite), corundum, silicon carbide, diamond, and titanium carbide have been found in primitive chondritic meteorites (5). These grains have survived because they are refractory and resistant to alteration. Identification is possible only because the isotopic compositions of these grains are significantly distinct from those of average solar system material. Interstellar grains provide insight into the fundamentals of nucleosynthesis, grain formation, and stellar evolution throughout the galaxy, and their study is a new frontier in meteoritics and astrophysical research.

Theoretical models predict grain lifetimes in the interstellar medium on the order of 10^8 years with shock waves (velocity, $V_s > 200 \text{ km s}^{-1}$) as the primary agent of destruction (3). Grains that survive are expected to be processed by (intergrain) collisional shock melting, vaporization, mixing, condensation, and prolonged ($\sim 10^8$ years) irradiation by energetic H and He nuclei. Grains that were originally anomalous can thus become isotopically and chemically "homogenized" (6, 7), yielding irradiated grains with approximately chondritic (solar) element abundances. [The average isotopic compositions of ga-

lactic cosmic rays and the interstellar medium are similar to that of average solar system material (6-8)]. Nonetheless, the grains found in primitive meteorites are evidence that isotopically anomalous interstellar grains were transported in the interstellar medium, were incorporated into the solar nebula, and survived postaccretionary parent-body processing that has altered the meteorites in which they are found.

If isotopically anomalous grains can survive, there may be an even larger population of interstellar grains in meteoritic materials, which have escaped detection because their homogenized compositions are not significantly different from those of solar system material. The logical place to search for such grains is in the most primitive meteoritic objects. Most meteorites are from main-belt asteroids, many of which have experienced significant postaccretionary alteration (9). Interplanetary dust particles (IDPs) are from dust-producing asteroids and comets (Fig. 1A) (10-12). Comets are believed to be the major reservoir of preserved solar nebula and interstellar grains within the solar system (1, 13). Most cometary IDPs are between 5 and 30 μm in diameter with chondritic (solar) bulk compositions (Table 1, rows 1 and 2) (14, 15). They are porous aggregates of single-mineral crystals, such as pyroxene, olivine, and Fe-rich sulfides; glass; carbonaceous material; and submicrometer polyphase grains, that is, grains composed of multiple minerals.

This report describes a specific class of polyphase grains that are a dominant component in most cometary IDPs. Although the occurrence of this type of grain within IDPs is well documented, the terminology used to describe them is confused. They have been called "tar balls," "granular units," "polyphase units," "microcrystalline aggregates," and "unequilibrated aggregates" (16-20). Here they are simply called GEMS (glass with embedded metal and sulfides), a term derived from both their min-

eralogy and their petrography (Fig. 1B). In addition to their homogenized (solar) bulk compositions, GEMS exhibit nanometer-scale compositional gradients that are consistent with exposure to ionizing radiation. Although the exposure could have occurred either in the solar nebula or in the interstellar medium, the inferred exposure ages of GEMS as well as their chemical and physical properties favor a presolar interstellar origin.

The IDPs, irradiated meteorite matrix, and lunar soil grains were embedded in epoxy and thin-sectioned with an ultramicrotome equipped with a diamond knife (17, 21). The electron-transparent thin sections (50 to 75 nm thick) were examined with a 200-keV analytical electron microscope (AEM) equipped with a solid-state x-ray detector and an electron energy-loss spectrometer (18, 22). Figure 2 shows a dark-field micrograph of a low Fe ($\sim 1\%$ by weight) pyroxene crystal (MgSiO_3) on the surface of IDP W7028C4 (Table 1, row 3). The linear features in the pyroxene are solar flare tracks, and the track density ($\sim 5 \times 10^{11} \text{ cm}^{-1}$) is consistent with a recent solar orbital exposure age of 10^4 to 10^5 years (23, 24). The rim is caused by solar wind damage, and both the tracks and the rim were acquired while the IDP was in solar orbit. Solar wind ions typically penetrate $\ll 1 \mu\text{m}$, whereas higher energy solar flare ions can penetrate to much greater depths in silicates (24, 25). Rims between 20 and 200

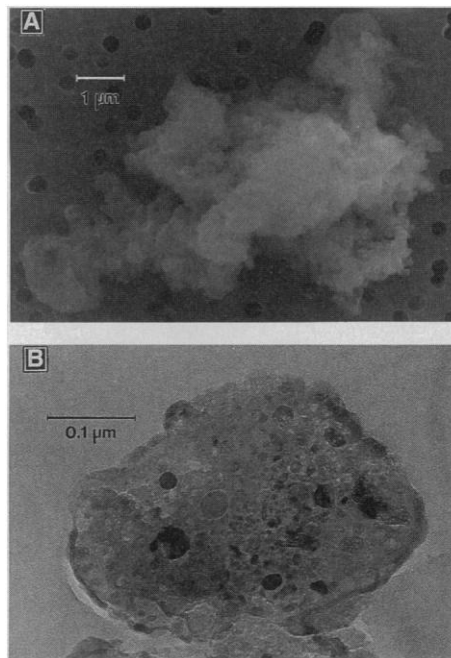


Fig. 1. (A) Secondary electron image of the cometary "chondritic porous" anhydrous interplanetary dust particle U2012C-21. (B) Bright-field image of a GEM composed of FeNi metal and Fe(Ni) sulfide crystals in glass [from (16)].

MVA, Incorporated, 5500 Oakbrook Parkway, #200, Norcross, GA 30093, USA.

nm thick are present on surface grains in most IDPs, generally with the thickest rims on crystals that exhibit the highest solar-flare track densities (17, 23). A similar relation exists in lunar soil grains (24, 25).

The compositions of the unspattered pyroxene crystal and its rim were measured by means of a quantitative thin-film energy-dispersive system (EDS) (22). Relative to the pyroxene, the rim is depleted in Mg and Ca and enriched in S, Si, and Fe (Table 1, rows 3 and 4). [I estimated the overall composition of the rim by collecting EDS spectra from multiple points (Table 1, row 4)]. There are compositional gradients in the rim (Fig. 3A and Table 1, rows 5 and 6). Using an electron probe ~20 nm in diameter, I performed a series of stepwise EDS analyses from the unspattered pyroxene crystal to the outer surface of the rim (Figs. 2 and 3A). At the crystal-rim interface, the rim composition is closest to that of the crystal but Mg and Ca are depleted (Table 1, row 5). Toward the surface of the rim, Mg is almost totally absent, and there is a 56% stoichiometric excess of O at the surface (Table 1, row 6).

A sample of fine-grained matrix from the Allende (CV3) chondritic meteorite was irradiated with 20-keV protons (total dose, 1.3×10^{18} ^1H per square centimeter) at normal incidence. [Allende matrix is compositionally and mineralogically analogous to IDPs in that it contains olivine, pyroxene, and Fe-rich sulfide grains (26)]. Figure 4 shows the radiation-damaged amorphous rim on an olivine crystal that was exposed to the ^1H beam. The composition of the

crystal confirms that it is stoichiometric olivine [$(\text{Mg}_{0.68}\text{Fe}_{0.32})_2\text{SiO}_4$] (Table 1, row 7). The amorphous rim is depleted in Mg, resulting in a 27% stoichiometric excess of O (Table 1, row 8). A ^1H -irradiated rim on a pyroxene (augite) crystal in Allende was also examined. [The amorphous silicate rim on the augite also contains nanometer-sized (FeNi)S inclusions.] Relative to the stoichiometric augite (Table 1, row 9), the rim is depleted in Mg and Ca (Table 1, row 10). If Ni and Fe are assigned as (FeNi)S and the remaining cations are assigned as oxides (that is, Al_2O_3 , MgO, SiO_2 , CaO, Cr_2O_3 , and FeO), there is a 29% stoichiometric excess of O in the rim on the pyroxene (Table 1, row 10).

Figure 5 shows four submicrometer grains within the matrices of two IDPs, U2012C-2I and U220A19. [Confirmation that U2012C-2I was captured from a cometary orbit was based on the degree to which it was pulse-heated during atmospheric entry (10, 27)]. The grain shown in Fig. 5A is an FeS crystal whose surfaces have been deeply eroded. Similarly eroded olivines, pyroxenes, and other crystals are common in cometary IDPs. Another FeS crystal (Fig. 5B) is even more deeply eroded and embedded in a matrix of silicate glass and finely divided FeS and FeNi metal crystals. This grain and those in Fig. 5, C and D, are GEMS.

Most GEMS are between 0.1 and 0.5 μm in diameter, their bulk compositions are within a factor of 3 of chondritic (solar) values for most major elements (Table 1, rows 1, 11, 12, and 15), and they are the

fundamental building blocks of cometary IDPs. The bulk composition of the grain in Fig. 5B is listed in Table 1, row 11. If S, Fe, and Ni are assigned as metal and sulfides and Mg, Al, Si, and Cr are assigned as oxides (MgO , Al_2O_3 , SiO_2 , Cr_2O_3), there is a 61% stoichiometric excess of O. Images of GEMS containing well-rounded FeS and FeNi crystals in glass are shown in Fig. 5, C and D. There is a systematic correlation between the textures and compositions of GEMS; those with the smallest FeNi and FeS inclusions and the highest glass contents (Fig. 5D) exhibit the highest glass enrichments in bulk O and depletions in Mg and other cations (Table 1, row 15).

Compositional profiles from two GEMS (Fig. 3, B and C) were obtained in a manner analogous to the sputtered rim profile from the pyroxene crystal (Fig. 3A). Because there is no unirradiated "substrate" in most GEMS, the electron beam (~20 nm in diameter) was first positioned at the center and then moved in steps toward the outer surface (Fig. 5C). The measured compositional trends in both GEMS mimic those of the (solar wind) irradiated rim on the pyroxene crystal (Fig. 3). In the first (Mg-rich) GEM, with a bulk O excess of 13% (Table 1, row 12), Mg becomes strongly depleted toward the surface (Fig. 3B and Table 1, rows 13 and 14). In the second GEM, with a bulk O excess of 86%, Mg and all cations except Si are depleted (relative to O) (Table 1, row 15); Si becomes depleted by a factor of 2 toward the surface (Fig. 3C), resulting in a 183% excess of O (Table 1, rows 16 and 17).

Table 1. Quantitative energy-dispersive x-ray analyses (atom percent, normalized). Major elements (rows 3 through 17) (>10 atom %), $\pm 5\%$ relative error; minor elements (1 to 10 atom %), $\pm 25\%$ relative error; trace elements (<1 atom %), $\pm 50\%$ relative error. Row 1, solar system abundances of the elements (C excluded) [from (14)]. Row 2, average composition of 90 anhydrous IDPs (C excluded) [from (15)]. Row 3, pyroxene crystal (Fig. 2), mean and standard deviation (σ) of five point-count analyses. Row 4, bulk compo-

sition of irradiated rim on pyroxene crystal (Fig. 2), mean and standard deviation (σ) of five point-count analyses. Row 5, base of rim (Fig. 2). Row 6, surface of rim (Fig. 2). Row 7, olivine crystal (Fig. 4). Row 8, irradiated rim on olivine crystal (Fig. 4). Row 9, augite crystal. Row 10, irradiated rim on augite crystal. Row 11, bulk composition of GEM (Fig. 5B). Row 12, bulk composition of GEM. Row 13, center of GEM. Row 14, surface of GEM. Row 15, bulk composition of GEM. Row 16, center of GEM. Row 17, surface of GEM.

Row	Element										Excess O (%)
	O	Mg	Al	Si	S	Ca	Cr	Mn	Fe	Ni	
1	49.7	10.3	0.9	11.5	5.7	0.3	0.3	0.2	20.0	1.1	
2	54.7	14.0	0.9	13.8	5.7	0.7	0.2		9.7	0.3	
3	59.4(2)	18.6(1)	0.9(0.25)	19.9(1.9)		0.4(0.05)	0.2(0.05)	0.2(0.03)	0.4(0.15)		3*
4	61.3(2.4)	10.9(3.4)	1.1(0.5)	24.4(1.5)	0.3(0.2)	0.1(0.07)	0.2(0.1)	0.1(0.05)	1.6(0.9)		4*
5	65.4	8.2	0.8	24.9		0.1	0.2	0.1	0.3		9*
6	75.2	0.5	0.6	22.9	0.3	0.1			0.4		56
7	57.0	16.2		13.7					13.1		0.5*
8	64.5	9.2	0.6	15.0					10.7		27
9	61.2	12.0	3.4	15.7		4.4	0.2		3.1		9*
10	61.0	6.0	2.3	13.0	3.4	0.4	1.5		11.1	1.3	29
11	61.9	2.9	0.8	16.9	6.1		0.3		11.1		61
12	56.2	22.3	0.6	13.3	3.2		0.1		4.2	0.1	13
13	52.9	24.6	1.2	12.1	3.9	0.2	0.3	0.2	4.4	0.2	3*
14	61.2	11.4	1.2	17.5	3.3	0.3	0.2	0.2	4.5	0.2	25
15	75.3	1.2	0.5	19.1	1.2		0.2	0.1	2.2	0.2	86
16	68.1	1.3	2.0	24.5	2.1		0.3	0.2	1.1	0.4	26
17	70.1	1.5		11.6	3.8				12.7	0.3	183

*Stoichiometric within experimental error.

A GEM texturally similar to that in Fig. 5D and with a bulk stoichiometric O excess of 84% was analyzed by electron energy-loss spectroscopy (EELS), a technique useful for investigating local atomic environments in solids (28). Figure 6 compares the electron energy-loss oxygen (O-K) core scattering ionization edge from the GEM with those of an (anhydrous) pyroxene (MgSiO_3) and (hydrated) talc [$\text{Mg}_6(\text{Si}_8\text{O}_{20})(\text{OH})_4$]. There is a pronounced shoulder (arrowed) on the low-energy side of the main ionization edge from the GEM (Fig. 6, curve A). Similar weaker shoulders were observed on the O-K edges from radiation-damaged amorphous rims on IDPs (Fig. 2), the Allende sample (Fig. 4), and some lunar soil grains. The magnitudes of the shoulders, relative to the main O-K edges, increase with O enrichment over stoichiometry. A shoulder precedes the main O-K edge from the hydrated talc but not the anhydrous pyroxene (Fig. 6, curves B and C).

Laboratory studies show that irradiation causes sputtering and the erosion of exposed surfaces (29). Sputtering can be nonstoichiometric in that atoms are not necessarily ejected in proportion to their relative abundances (30). An irradiated surface initially becomes enriched in heavy atoms because light atoms are more efficiently backscattered out of the target (30, 31). However, superimposed on this trend are the effects of the bombarding ions (mass, energy, incidence angle, fluence), recoil mixing (reimplantation of sputtered atoms), diffusion, and various properties of the target itself (for example, redox potentials and bond strengths) (29–31). Net enrichments of light versus

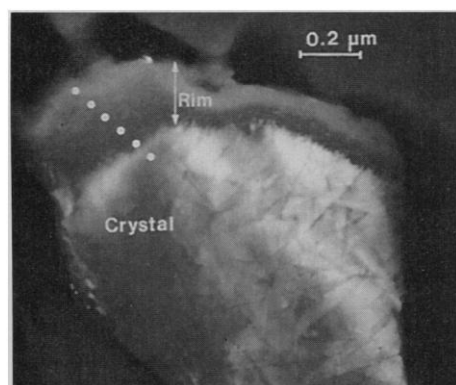


Fig. 2. Dark-field electron micrograph of a pyroxene (MgSiO_3) crystal on the surface of IDP W7027C4. The linear features in the crystal are solar flare tracks (density of $\sim 10^{11} \text{ cm}^{-2}$), indicating a solar orbital exposure age of $\sim 10^4$ years (23). The rim results from irradiation by solar wind ions. Compositions of the crystal and rim are given in Table 1, rows 3 through 6. White dots illustrate the approximate positions of the electron probe during the acquisition of a compositional profile (Fig. 3A).

heavy atoms in irradiated objects may be controlled by recoil implantation and total ion fluence (31). Although light elements are preferentially sputtered, they are also more efficiently recoil-implanted into deeper regions of the target by incoming ions. After a small ion fluence, a surface layer enriched in heavy atoms develops, while reimplanted lighter atoms accumulate at greater depths. After a prolonged ion fluence, the surface migrates downward to the light element-enriched region by sputter erosion. Thus, irradiated grains highly enriched in light elements, such as O, may have been exposed to prolonged ion fluences.

Irradiation by H and He ions is an important erosional process acting on solids throughout the interstellar and interplanetary medium, and some extraterrestrial materials exhibit evidence of this erosion (3, 6, 7). Soil grains on the lunar surface ac-

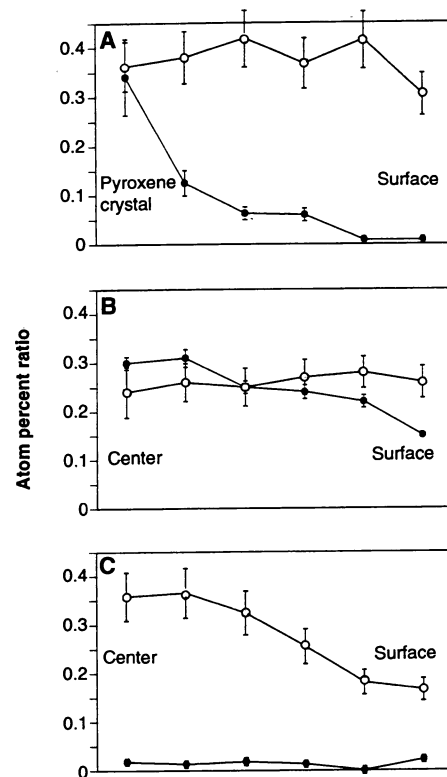


Fig. 3. Compositional profiles of irradiated silicate grains; atom abundances of Mg (filled circles) and Si (hollow circles) relative to O. (A) Irradiated rim (in Fig. 2) obtained by collection of stepwise x-ray spectra from the pyroxene crystal (left side of the plot) to the outer edge of the rim (right side). (B) GEM (with 12% bulk O excess) obtained by collection of stepwise spectra from the center of the grain (left) to the outer surface (right) (see also Table 1, rows 12 through 14). (C) GEM (with 86% bulk O excess) from the center (left) to the outer surface (right) (Table 1, rows 15 through 17). The (2σ) error bars were assessed by repetitive EDS point-count analyses of thin-film standards and the pyroxene crystal (Fig. 2; Table 1, row 3).

quire amorphous rims resulting from exposure to solar wind H and He as well as nuclear tracks from solar flares (24, 25), and IDPs in solar orbit acquire solar wind-irradiated rims and implanted solar flare tracks

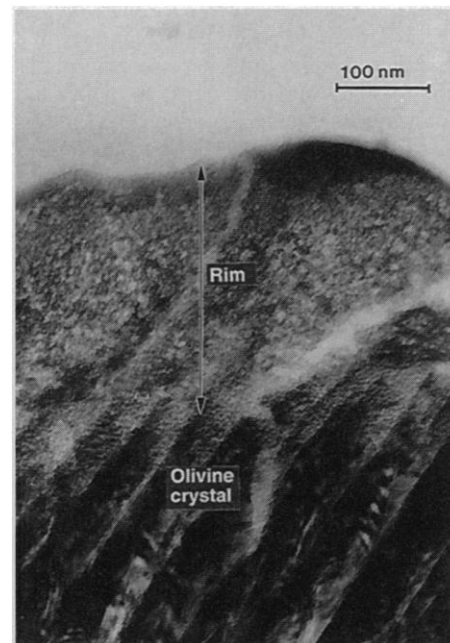


Fig. 4. Bright-field micrograph of a thin section ($<100 \text{ nm}$ thick) of the ^1H -irradiated surface of an olivine crystal in Allende (CV3) meteorite matrix. Compositions of the olivine crystal and rim are given in Table 1, rows 7 and 8.

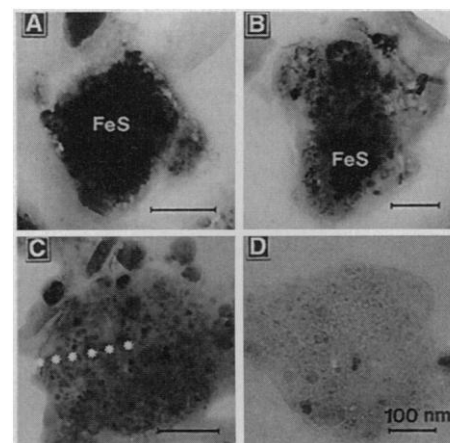


Fig. 5. Bright-field electron micrographs of irradiated grains within the matrices of anhydrous IDPs. Relative irradiation doses increase from (A) through (D). (A) An FeS crystal with etched surfaces (IDP U2012-21). (B) GEM containing a deeply etched FeS crystal (U2012C-21). (C and D) GEMs with progressively longer exposure ages (U220A19). Note the increased rounding and decreased grain size and definition with exposure age. Stars in (C) illustrate the approximate diameter and positions of the electron probe during acquisition of the compositional profiles (for example, Fig. 3, B and C). Scale bars, 100 nm.

(Fig. 2) (23). Surface rims on IDPs and some lunar soil grains are depleted in Mg and Ca, enriched in O, and invariably enriched in S, Fe, and Ni (Table 1, rows 3 through 6). These same chemical effects in rims on the ^1H -irradiated meteorite sample (Fig. 4) result from exposure to ionizing radiation (Table 1, rows 7 through 10). In silicates, the irradiation effects are dynamic in that silicate crystals become amorphous while crystalline inclusions of metal and sulfides accumulate (25, 29, 31–33). Depending on the target (silicate) composition, ion irradiation first strips cations (for example, Mg and Ca) with the weakest bond strengths (34). When these cations are depleted, more strongly bound cations (for example, Si) are stripped. The net result is an irradiated object with a stoichiometric “excess” of O.

The chemical state of the excess O in irradiated silicates is of fundamental importance because, in the absence of a compensating phenomenon, selective removal of cations from silicates must produce dangling O bonds and charge imbalance. Prolonged irradiation implants saturation levels of H and He in silicates and, although H is difficult to measure directly by electron microscopy, H could provide the necessary charge balance as hydroxyl ($-\text{OH}$) ions. The low energy shoulder on the O-K edges from GEMS (Fig. 6, curve A) and other irradiated silicates suggests that the implanted H and excess O are present as $-\text{OH}$ because the same shoulder is present on the O-K edge from talc [$\text{Mg}_6(\text{Si}_8\text{O}_{20})(\text{OH})_4$] (Fig. 6, curve B) and brucite [$(\text{Mg}(\text{OH})_2)_2$]. [Iron-free talc and brucite were analyzed because the O-K edges from iron oxides, (such as Fe_3O_4) and other transition-metal oxides also exhibit a pre-edge shoulder (35)]. Shoulders are not observed on the

O-K edges from pyroxene (Fig. 6, curve C) and other anhydrous silicates (36).

GEMS within cometary IDPs (Fig. 4) also exhibit the effects of irradiation, but the magnitudes of the cation depletions, the nonstoichiometry of O, and the accumulations of Fe, Ni, and S (Table 1, rows 11 through 17) relative to the ($\sim 10^4$ -year-old) solar wind-damaged rims on the surfaces of IDPs (Table 1, rows 4 through 6) suggest that some GEMS were irradiated on time scales of $\gg 10^4$ years. Moreover, the spheroidal morphologies of the GEMS and their embedded grains are typical of grains exposed to prolonged irradiation (25, 37). Although specific details of the irradiation flux regime are unknown, the inferred exposure ages of GEMS are qualitatively consistent with theoretical ($\sim 10^8$ years) exposure lifetimes of interstellar grains (2, 3, 6, 7). Because the distribution of GEMS is not surface-correlated, that is, they are dispersed throughout the interiors of IDPs, their exposures must have been preaccretional. Their homogenized compositions are consistent with prolonged irradiation in an environment where processing by irradiation, sputtering, recoil mixing, crystal growth, and vitrification produced grains with approximately cosmic (chondritic) element abundances. The interstellar medium is such an environment (1–3, 6, 7). GEMS may have been a major component of the submicrometer dust grains analyzed by instruments on the Giotto and Vega spacecraft during the 1986 comet Halley encounters. The distribution of the Mg/Si ratio versus the Fe/Si ratio in Halley's dust is unlike that seen in primitive fine-grained meteorites and most IDPs, and it is difficult to explain in terms of a simple mixture of mineral grains (38). However, the distribution of the Mg/Si ratio versus the Fe/Si ratio in IDPs dominated by GEMS is very similar to that found in comet Halley's dust (20, 38).

The characteristic chemical signature of solar wind irradiation on the surfaces of IDPs (Fig. 3A) applies equally to lunar soil grains. Although there is compelling evidence that some amorphous rims on lunar soil grains are caused by solar wind damage, condensed impact-generated vapors also deposit on lunar grains (24, 25, 32, 33). The relative contributions of these processes are under investigation (32). The vapor deposition hypothesis is based on observations similar to those reported in this report, specifically that the rims are enriched in certain cations (S and Si) and contain nanometer-size inclusions of Fe and FeS. However, similar chemical effects in rims on IDPs and ^1H -irradiated silicates that were not exposed to regolith vapors establish that solar wind irradiation can effect significant chemical changes in silicate grains (Figs. 2 and 4 and Table 1, rows 4 through 10).

Stoichiometric excesses or depletions of O measured in rims on lunar soil grains could clarify the relative contributions or solar wind damage versus vapor deposition. [Condensed rims are unlikely to be enriched in O because silicate glasses formed from vapors should be stoichiometrically depleted in O (39)].

GEMS are abundant in cometary IDPs along with grains that do not appear to have been preaccretionally irradiated (predominantly single crystals of silicates and Fe-rich sulfides). Cometary IDPs are expected to contain both solar nebula and interstellar dust grains (13). [Nonsolar $^3\text{He}/^4\text{He}$ ratios measured in U2012C-2I (Fig. 1A) and other cometary IDPs suggest an interstellar irradiation component (27)]. Solar nebula grains in comets are unlikely to have been exposed to prolonged irradiation, although intense short-term exposure during a more active phase of the early sun cannot be ruled out. However, interstellar grains in comets were inevitably subjected to prolonged preaccretional irradiation. Furthermore, the submicrometer sizes, chondritic (solar) compositions, amorphous silicate structures, and inferred exposure ages of GEMS are consistent with those of silicate grains in the interstellar medium (2–4, 6, 7, 40). Other preaccretionally irradiated interstellar grains may exist in meteorites in which isotopically anomalous grains have already been found. However, grains rendered amorphous by irradiation are particularly vulnerable to alteration with reported hydration rates enhanced by as much as 10^3 times (41). Meteorites are more suitable as sources of interstellar grains because of their larger masses and grain sizes, but they are also more altered than some anhydrous IDPs.

Electron microscopy may provide access to a whole new population of interstellar grains in IDPs. The existing capability of determining both the chemistry and the precise location of submicrometer grains may make complimentary isotope measurements with the ion microprobe possible.

REFERENCES AND NOTES

1. E. P. Ney, *Science* **195**, 541 (1977).
2. J. S. Mathis, *Rep. Prog. Phys.* **56**, 605 (1993).
3. G. C. Seab and M. J. Shull, in *Interrelationships Among Circumstellar, Interstellar, and Interplanetary Dust*, J. A. Nuth and R. E. Stencel, Eds. [National Aeronautics and Space Administration (NASA) Conference Publication 2403, Washington, DC, 1986], p. 37.
4. S. H. Kim, P. G. Martin, P. D. Hendry, *Astrophys. J.* **422**, 164 (1994).
5. T. J. Bernatowicz, P. C. Gibbons, R. S. Lewis, *ibid.* **359**, 246 (1990); E. Anders and E. Zinner, *Meteoritics* **24**, 490 (1993); U. Ott, *Nature* **364**, 25 (1993).
6. J. A. Nuth, in *Meteorites and the Early Solar System*, J. F. Kerridge and M. S. Matthews, Eds. (Univ. of Arizona Press, Tucson, 1988), p. 984.
7. J. A. Nuth and J. H. Hecht, *Astrophys. Space Sci.* **163**, 79 (1984).
8. M. E. Wiedenbeck, *Adv. Space Res.* **4**, 15 (1984).
9. H. Y. McSween and S. M. Richardson, *Geochim.*

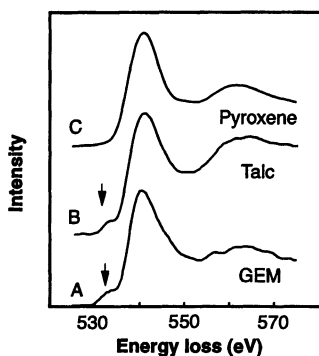


Fig. 6. Electron energy-loss oxygen (O-K) core scattering edges following a point spread function correction, deconvolution, and background subtraction. Energy resolution (measured at 284 eV) is ~ 0.75 eV. (Curve A) GEM (with 84% bulk O excess). (Curve B) Talc [$\text{Mg}_6(\text{Si}_8\text{O}_{20})(\text{OH})_4$]. (Curve C) Pyroxene [enstatite (MgSiO_3)].

- Cosmochim. Acta* **41**, 1145 (1977); T. E. Bunch and S. Chang, *ibid.* **44**, 1543 (1980); G. P. Meeker, G. J. Wasserburg, J. T. Armstrong, *ibid.* **47**, 707 (1983); M. E. Zolensky, W. C. Bourcier, J. L. Gooding, *Icarus* **78**, 411 (1989).
10. D. E. Brownlee et al., *Lunar Planet. Sci. Conf. XXIV*, 205 (1993); D. E. Brownlee et al., *ibid.* **XXV**, 185 (1994).
 11. M. V. Sykes, L. A. Lebofsky, D. M. Hunten, F. Low, *Science* **232**, 1115 (1986); J. P. Bradley and D. E. Brownlee, *ibid.* **251**, 549 (1991); A. A. Jackson and H. A. Zook, *Icarus* **97**, 70 (1992).
 12. IDPs are collected in the stratosphere at an altitude of 20 to 25 km by NASA U2 and RB57 aircraft. See D. E. Brownlee, *Annu. Rev. Earth Planet. Sci.* **13**, 147 (1985); S. A. Sandford, *Fundam. Cosmic Phys.* **12**, 1 (1987).
 13. J. M. Greenberg, in *Comets*, L. L. Wilkening, Ed. (Univ. of Arizona Press, Tucson, 1982), p. 131; F. L. Whipple, in *The Zodiacal Light and the Interplanetary Medium*, J. L. Weinberg, Ed. (Office of Technology Utilization, NASA, Washington, DC, 1967), pp. 409–426; J. S. Dohnanyi, in *Cosmic Dust*, J. A. M. McDonnell, Ed. (Wiley-Interscience, New York, 1978), pp. 527–605; M. S. Hanner, J. A. Hackwell, R. W. Russel, D. K. Lynch, *Icarus*, in press.
 14. E. Anders and M. Ebihara, *Geochim. Cosmochim. Acta* **46**, 2363 (1984).
 15. At least three classes of IDPs with approximately chondritic (solar) bulk compositions are recognized [see S. A. Sandford and R. M. Walker, *Astrophys. J.* **291**, 838 (1985); J. P. Bradley, *Geochim. Cosmochim. Acta* **52**, 889 (1988)]. The IDPs reported here belong to the anhydrous "chondritic porous" (CP), typically pyroxene-rich but some with significant amounts of olivine (L. S. Schramm, M. M. Wheelock, D. E. Brownlee, *Meteoritics* **24**, 99 (1989)). Most identified cometary IDPs belong to the CP class (10). Isotopic anomalies have been found in 13 IDPs, about 40% of the particles so far studied; D/H enrichments (associated with C) and ¹⁵N enrichments suggest the survival of an organic component from cold interstellar clouds [see K. D. McKeegan, R. M. Walker, E. Zinner, *Geochim. Cosmochim. Acta* **49**, 1971 (1985); F. J. Stadermann, R. M. Walker, E. Zinner, *Meteoritics* **24**, 327 (1989)]. Enrichments of D and ¹⁵N have also been found in meteorites, but anomalies in C, O, Mg, and Si that are found in meteorites have yet to be found in chondritic IDPs. The small sizes of IDPs and their extreme submicrometer-scale heterogeneity complicate detection of isotope anomalies.
 16. J. P. Bradley, S. A. Sandford, R. M. Walker, in (6), p. 861.
 17. J. P. Bradley and D. E. Brownlee, *Science* **231**, 1542 (1986).
 18. J. P. Bradley, *Geochim. Cosmochim. Acta* **58**, 2123 (1994).
 19. F. J. M. Rietmeijer, *Proc. Lunar Planet. Sci. Conf.* **19**, 513 (1989); in *Analysis of Interplanetary Dust*, M. E. Zolensky, F. J. M. Rietmeijer, G. J. Flynn, Eds. (American Institute of Physics, New York, 1994), p. 231.
 20. J. P. Bradley, H. J. Humecki, M. S. Germani, *Astrophys. J.* **394**, 643 (1992).
 21. J. P. Bradley, *Geochim. Cosmochim. Acta* **52**, 889 (1988).
 22. Data were acquired with the use of a 200-keV JEOL (Peabody, MA) 2010 AEM equipped with a Noran TN5500 x-ray EDS sensitive to elements with atomic number $Z > 5$, and a Gatan (parallel detection) electron energy-loss spectrometer. A thin-film procedure was used in measuring the compositions [see G. Cliff and G. W. Lorimer, *J. Microsc.* **103**, 203 (1975)]. Experimental EDS correction (K) factors were derived from analyses of thin-film standards [see J. P. Bradley, M. S. Germani, D. E. Brownlee, *Earth Planet. Sci. Lett.* **93**, 1 (1989); M. S. Germani, J. P. Bradley, D. E. Brownlee, *ibid.* **101**, 162 (1990)].
 23. J. P. Bradley, D. E. Brownlee, P. Fraundorf, *Science* **226**, 1432 (1984); K. Thiel, J. P. Bradley, R. Spohr, *Nucl. Tracks Radiat. Meas.* **19**, 708 (1991).
 24. R. L. Fleischer, P. B. Price, R. M. Walker, *Nuclear Tracks in Solids: Principles and Applications* (Univ. of California Press, Berkeley, 1975).
 25. J. Bibring et al., *Science* **175**, 753 (1972); M. Maurette and P. B. Price, *ibid.* **187**, 121 (1975).
 26. H. Y. McSween, *Geochim. Cosmochim. Acta* **47**, 1777 (1977).
 27. A. O. Nier and D. J. Schlutter, *Meteoritics* **28**, 675 (1993).
 28. J. Taftø and J. Zhu, *Ultramicroscopy* **9**, 349 (1982); P. E. Batson, *Nature* **366**, 727 (1993); D. A. Muller, Y. Tzou, R. Raj, J. Silcox, *ibid.*, p. 725.
 29. J. C. Pivin, *J. Mater. Sci.* **18**, 1267 (1983).
 30. D. M. Paruso, W. A. Cassidy, B. W. Hapke *Proc. Lunar Planet. Sci. Conf.* **9**, 1711 (1978); M. F. Hochella, J. R. Lindsay, V. G. Mossotti, C. M. Eggleston, *Am. Mineral.* **73**, 1449 (1988); R. Kelly, I. Bertóti, A. Miotello, *Nucl. Instrum. Methods Phys. Res. B* **80/81**, 1154 (1993).
 31. P. Sigmund, *J. Appl. Phys.* **50**, 7261 (1979).
 32. L. P. Keller and D. S. McKay, *Science* **261**, 1305 (1993); *ibid.* **264**, 1780 (1994); T. J. Bernatowicz, R. H. Nichols, C. M. Hohenberg, *Lunar Planet. Sci. Conf. XXIV*, 105 (1994); T. J. Bernatowicz, R. H. Nichols Jr., C. M. Hohenberg, M. Maurette, *Science* **264**, 1779 (1994); B. Hapke, W. Cassidy, E. Wells, *ibid.*, p. 1779.
 33. J. F. Kerridge and I. R. Kaplan, *Proc. Lunar Planet. Sci. Conf.* **9**, 1687 (1978); B. Hapke, W. Cassidy, E. Wells, *Moon* **13**, 339 (1975); J. F. Kerridge, *Lunar Planet. Sci. Conf. XXI*, 301 (1991).
 34. F. Liebau, *Structural Chemistry of Silicates: Structure, Bonding, and Classification* (Springer-Verlag, New York, 1985).
 35. L. A. Grunes, R. D. Leapman, C. N. Wilker, R. Hoffmann, A. B. Kunz, *Phys. Rev. B* **25**, 7157 (1982).
 36. M. T. Otten and P. R. Buseck, *Phys. Chem. Minerals* **14**, 45 (1987).
 37. J. P. Bibring et al., *Earth Planet. Sci. Lett.* **22**, 205 (1974).
 38. D. E. Brownlee, M. M. Wheelock, S. Temple, J. P. Bradley, J. Kissel, *Lunar Planet. Sci. Conf. XVIII*, 133 (1987); M. E. Lawler, D. E. Brownlee, S. Temple, M. M. Wheelock, *Icarus* **80**, 225 (1989).
 39. J. A. Nuth and B. Donn, *J. Geophys. Res.* **88**, A847 (1983).
 40. D. K. Aitken, P. F. Roche, C. H. Smith, S. D. James, J. H. Hough, *Mon. Not. R. Astron. Soc.* **230**, 629 (1988); A. G. G. M. Tielens, in *From Miras to Planetary Nebulae: Which Path for Stellar Evolution*, M. O. Mennessier, Ed. (Editions Frontiers, Gif sur Yvette, 1990), p. 186.
 41. J. C. Dran et al., *Nucl. Instrum. Methods B* **1**, 557 (1984).
 42. This research was supported by NASA (contract NASW 4832). I thank T. VanderWood and R. Wilson for technical assistance and D. Brownlee and T. Bernatowicz, D. Burnett, L. Keller, M. Maurette, and K. Thiel for critical discussions. I thank D. Brownlee for supplying the image in Fig. 1A.

24 January 1994; accepted 24 June 1994

Impact Crater Densities on Volcanoes and Coronae on Venus: Implications for Volcanic Resurfacing

Noriyuki Namiki* and Sean C. Solomon

The density of impact craters on large volcanoes on Venus is half the average crater density for the planet. The crater density on some classes of coronae is not significantly different from the global average density, but coronae with extensive associated volcanic deposits have lower crater densities. These results are inconsistent with both single-age and steady-state models for global resurfacing and suggest that volcanoes and coronae with associated volcanism have been active on Venus over the last 500 million years.

Volcanic features are widely distributed over the surface of Venus (1), and their ages provide critical information on the magmatic budget of the planet. However, the generally low density of impact craters on Venus, a result of atmospheric shielding (2, 3), has prevented a comparison of crater retention ages among small regions (4) and contributes to the controversy over whether a catastrophic (2) or an equilibrium model (3) better describes the global resurfacing history. The spatial diversity of the crater distribution has nonetheless been addressed by grouping areas by latitude or longitude (2), radar cross section (3), elevation (5), or terrain type (6). Following this practice, we have integrated the areas and cratering records for large volcanoes and for coronae

(7) on Venus, and we assess here the implications of the results for volcanism and global resurfacing.

We made use of a database of 841 impact craters classified according to the extent of tectonic deformation and of embayment or partial covering by volcanic material (5, 8). A database for 175 volcanoes at least 50 km in diameter (9), compiled from Magellan images and a published map (1), includes radius and relief of the topographic edifice and the dimensions of the radial flow apron. A database for 358 coronae (10) includes a classification by feature type and extent of interior volcanism. There are 51 features listed in both the volcano and corona databases, because in many coronae there are associated volcanic centers.

For each large volcano, we ascertained from the databases the presence of one or more impact craters on the edifice or flow apron, and from Magellan radar images we determined superposition relations (Fig. 1). We included the edifice and discernible radial flows in calculating the area of each

N. Namiki, Department of Earth, Atmospheric, and Planetary Sciences, Massachusetts Institute of Technology, Cambridge, MA 02139, USA.
S. C. Solomon, Department of Terrestrial Magnetism, Carnegie Institution of Washington, 5241 Broad Branch Road, NW, Washington, DC 20015, USA.

*To whom correspondence should be addressed.